Journal of Fluids and Structures 133 (2025) 104259

Contents lists available at ScienceDirect

Journal of Fluids and Structures

journal homepage: www.elsevier.com/locate/jfs

Dynamic loading of two side-by-side tidal stream turbines in regular waves

J. McNaughton [a,b], F. Zilic de Arcos [a,c], C.R. Vogel [a], R.H.J. Willden [a,*]

[a] Department of Engineering Science, University of Oxford, UK
[b] Maritime Research Institute Netherlands (MARIN), Netherlands
[c] Université Le Havre Normandie, France

ARTICLE INFO

Keywords:
Tidal turbines
Hydrodynamics
Regular waves
Dynamic loading

ABSTRACT

This paper investigates the dynamic loading of two side-by-side 1.2 m diameter tidal stream turbines tested experimentally in currents with regular waves. By towing the turbines through a tank against head waves we explore the influence of tip-speed ratio, wave amplitude and wave frequency, on the mean and unsteady rotor and blade loads. Turbine mean power and thrust coefficients in waves agree well with the steady flow coefficients recorded without waves. The dynamic power and thrust coefficients describe paths forming hysteresis loops around mean values when presented against tip-speed ratio defined based on instantaneous rotor-averaged flow speed. Single frequency harmonic fits provide reasonable fits to rotor loads enabling the assessment of loading phase with respect to incident waves. Rotor fluctuating loads increase with wave amplitude and tip-speed ratio, but decrease with wave frequency, with rotor torque showing greater sensitivity to wave conditions than thrust. Analysis of blade root bending moments as a function of wave phase and blade azimuth reveals that flapwise and edgewise load maxima and minima occur in advance of the crests and troughs of the approaching waves, but that the azimuthal locations at which blades experience maxima and minima are functions of wave frequency. Contrary to expectations blade loading is found to be maximum when blades are approximately horizontal which we attribute to spanwise correlation of wave orbital kinematics along blades. As wave frequency is increased, blade load maxima and minima occur closer to top dead centre due to increased vertical decay of wave orbitals. Peak flapwise and edgewise blade loads are found to occur on blade upstrokes and downstrokes respectively which we attribute to the contribution of the vertical component of wave orbitals and rotor-rotor interference. Differences in blade loads of the side-by-side turbines are attributed to hydrodynamic interactions due to the close quarter-diameter spacing between rotors.

1. Introduction & motivation

In order to be able to produce effective designs for tidal stream turbines, it is imperative that we understand and are able to quantify and model the dynamic performance and loads experienced by these devices in unsteady flow environments. Turbines are exposed to sources of unsteadiness including deterministic loading fluctuations due to the cyclical passage of blades through sheared velocity profiles and more stochastic unsteady loading from turbulence and surface waves (Adcock et al., 2021). In this

* Corresponding author.
E-mail addresses: j.mcnaughton@marin.nl (J. McNaughton), federico.zilic@eng.ox.ac.uk (F. Zilic de Arcos), christopher.vogel@eng.ox.ac.uk (C.R. Vogel), richard.willden@eng.ox.ac.uk (R.H.J. Willden).

https://doi.org/10.1016/j.jfluidstructs.2024.104259
Received 7 June 2024; Received in revised form 25 October 2024; Accepted 19 December 2024
Available online 3 February 2025

paper we concentrate on the influence of surface waves. Whilst most previous studies have examined the influence of waves on the time-averaged performance of tidal turbines, here we also examine dynamic performance coefficients, and the variation of turbine blade loads with respect to wave and blade phase. Additionally, we seek to investigate to what extent the turbine's behaviour through waves can be approximated by quasi-steady assumptions on performance coefficients, where it is assumed that a dynamic change in tip-speed ratio (TSR) results in a change in power and thrust coefficients that track steady-state curves.

Tidal turbine rotors positioned in the vicinity of the free surface are affected by the presence of surface waves. The height and wavelength of regular waves determine the intensity of velocity fluctuations through the water column. In deep or transitional depths, wave kinematics decay with depth, with shorter waves decaying faster than longer waves. The kinematics are additionally affected by wave amplitude, with larger amplitudes driving stronger flow fluctuations. As the blades rotate in the presence of surface waves, they experience a spatially and temporally varying velocity field that can induce substantial load and power fluctuations (Draycott et al., 2020). Due to the depth decay of wave kinematics, turbine load fluctuations depend not only on the wave parameters, amplitude and wavelength, and operation of the turbine, speed and pitch, but also on the rotor submergence depth (Guo et al., 2018; Dufour et al., 2022).

One of the first experimental studies on tidal turbines in waves was performed by Barltrop et al. (2007), testing a three-bladed 0.4 m diameter tidal rotor in a towing tank. The turbine was studied under different wave, towing, and rotational speed configurations. Their results showed that waves induce substantial power and thrust fluctuations while mean loads remain largely unaffected. Similar conclusions were reached by Faudot and Dahlhaug (2012), Gaurier et al. (2013), Luznik et al. (2013), Galloway et al. (2014), and Guo et al. (2018), in studies that involved different rotors, experimental facilities, and testing conditions.

Literature suggests that waves are one of the dominant sources of unsteady loading on tidal rotors (Scarlett et al., 2019). Galloway et al. (2014), for example, describes an increase of up to 175% in the median flapwise root bending moment and 100% increase of the median edgewise root moment, while (Draycott et al., 2019) reported maximum thrust and torque increasing by up to 65% and 160%, respectively, with respect to mean values.

Blades positioned near the top dead centre (TDC) are expected to sample the strongest flow fluctuations due to their proximity to the free surface and the nature of wave kinematics decay. The stronger kinematics near the free surface were related to larger thrust and power fluctuations for blades near TDC in the numerical study of Zilic de Arcos et al. (2023b), with the largest thrust and power fluctuations on the blades of a 20 m diameter tidal rotor shown close to the TDC position. Dufour et al. (2022), however, found different results in an experimental campaign where two different rotors were tested under the influence of currents and waves and at two submergence depths. Their study showed that peak fluctuations in root bending moments occurred around 10° from bottom dead centre but this was attributed to a strong vertical velocity shear, increasing with depth, rather than to the influence of surface waves alone.

The experimental campaign of Lust et al. (2013) explored the phase between regular waves and integrated thrust, torque, and rotational speed of a tidal turbine. They observed all measured quantities, except torque, to have maximum and minimum values at the wave crest and trough, respectively. Torque, however, lagged compared to the other quantities, which was attributed to the influence of vertical wave kinematics. Similar observations were made by Guo et al. (2018) with respect to wave phase for maxima and minima turbine loads, with a small lag in the integrated thrust and torque reported with respect to wave elevations.

A gap observed in the literature is the lack of measurement in the incident and disturbed wave fields. Additionally, inconsistency in the positioning of wave probes to measure and quantify onset reference waves provides further uncertainty to the wave conditions experienced by the rotors and thus conclusions that can be drawn. For example Lust et al. (2013) used two optical wave sensors, one placed at the rotor plane and two diameters to the side of the turbine centreline, with the other approximately one diameter upstream and next to the tank wall. Draycott et al. (2019) used a single wave gauge positioned over the turbine, as did Allmark et al. (2021) but with theirs offset to the side of the rotor, whilst Guo et al. (2018) positioned their wave probe 4.5 m (5.6 diameters) upstream of the turbine. None of these studies quantify the impact of the turbine on the approaching free surface waves or on them as they pass over the turbines, whilst the wave diffraction caused by the rotor suggests that conclusions drawn about the effects of wave phase on rotor loads could be affected by the positioning of the probes.

Li et al. (2021), Zilic de Arcos et al. (2023a), Stallard et al. (2023), and Ouro et al. (2024) studied different tidal rotors under the combined effects of currents and regular waves using Computational Fluid Dynamics (CFD) simulations with an embedded actuator line model (Sørensen and Shen, 2002; Zormpa et al., 2025). The numerical studies agree with the experimental observation of the invariance of time-averaged loads, and the significance of load and power fluctuations. These studies also demonstrate that waves increase wake mixing, generally driving faster rates of wake recovery, when compared to cases without waves. Of the studies above, only Li et al. (2021) highlighted the impact of the rotor on the free surface, indicating the presence of a bulge and depression upstream and downstream of the rotor, with changes to mean free surface elevation two orders of magnitude below the amplitude of their surface waves.

The studies discussed above are focused on single rotor configurations. Multiple rotors operating within cross-stream fences are known to interact with each other, increasing the potential for power extraction (Nishino and Willden, 2012). These constructive interference effects were demonstrated experimentally by McNaughton et al. (2022), where flume experiments show an increase in power of up to 11% with an attendant increase in thrust of 5% for two 1.2 m diameter tidal rotors in co-planar fence configuration. McNaughton et al. (2023) used the same two rotors positioned in a co-planar fence positioned normally to the side wall of a towing tank, so as to act as a symmetry plane, to mimic the performance of a co-planar four-rotor array. Their study demonstrated azimuthal variations in edgewise and flapwise bending moments that increased as inter-turbine spacing was reduced and varied between in-board and out-board rotors, showing up to 5%–10% higher flapwise and edgewise bending moments as the

blades passed next to the neighbouring rotor. Despite these interference effects being widely described in literature, no studies have focused, to the best of our knowledge, on the effects of waves or other transient flow phenomena on multi-rotor fence configurations.

In order to gain further insight into the dynamic loads experienced by tidal turbines in currents with head-waves we perform tow tank tests of two turbines in side-by-side arrangement. We take particular care to measure the impact of the turbines on the upstream flow and to the determination of the wave conditions experienced at the rotor plane. By using rotor models with root flexures instrumented to record bending moments we are able to ascertain the dynamic variation of edgewise and flapwise bending moments as the waves pass over the turbines, and how these loads are a function of the azimuthal position of the blades and the incident wave phase. The experimental procedure is outlined in Section 2, with analysis procedure described in Section 3 and results discussed in Section 4.

2. Methodology

2.1. Test facility

The tests in this study were performed using QinetiQ's Haslar towing tank in Portsmouth (QinetiQ, 2018). The tank is 12.2 m wide, 5.4 m deep and 270 m total length, with a usable testing length of around 150 m. The carriage supports a maximum towing load of 5 kN and can achieve speeds of up to 12 m/s, although the current tests were limited to a carriage speed $U_C = 1$ m/s in order to moderate the turbine loads and rotational speeds to within acceptable ranges. Wave makers operate at one end of the tank, with beaches for wave absorption at the dock end of the tank. For the purpose of these tests the turbines were towed from the beach end towards the wave makers, and hence all waves are head-waves aligned with the imposed current direction.

2.2. Twin turbines

Two turbines of identical design were used in this study. They have a rotor diameter, d, of 1.2 m and were positioned at a constant 1 m hub depth, *i.e.*, 0.4 m minimum tip clearance, from the mean free surface level. Global blockage, defined as the ratio between the swept area of the two rotors to the tank cross-sectional area, was 3.4%. The turbines were rigidly supported vertically beneath the towing carriage and positioned side-by-side with a 0.3 m ($0.25d$) inter-turbine tip-to-tip spacing. The turbine layout was symmetrical about the tank mid-plane, except for the direction of rotation, which was the same for both turbines; positive about the x-axes for each turbine where the positive x-direction points along the length of the tank in the direction of towing. The turbine submersion depth and inter-turbine spacing were set to match previous experiments; in a similar towing tank where turbine performance without waves was investigated (McNaughton et al., 2023); and in a recirculating flume where performance in sheared flow with upstream turbulence was investigated (McNaughton et al., 2022).

The turbines are controlled to achieve an operator-specified rotational speed, and measurements made of rotor thrust, torque and speed, as well as blade root bending moments in flapwise and edgewise directions. Details of the instrumented drivetrain and rotor are given in McNaughton et al. (2023). The hydrodynamic design process for the blades is described in Cao (2020). A previous experimental campaign in the SSPA towing tank in Gothenburg, Sweden, demonstrated that the performance of these rotors was independent of Reynolds number at tow speeds at or above 0.9 m/s for tip-speed ratios in the range of 5.5 to 8.0 (McNaughton et al., 2023).

We present experimental results over a range of wave amplitudes, 0.02–0.1 m, and frequencies, 0.3 to 0.7 Hz. These ranges were chosen according to the capabilities of the wave paddles in the facility but also from consideration of Froude scaling. Based on Froude scaling of the turbine to a commercial scale device of c. 20 m diameter, the tested wave parameters infer full-scale wave heights of up to 1.7 m and a range of wave periods between 6 and 14 s, which are representative of ocean conditions in which a tidal turbine may operate.

2.3. Testing procedure

The same testing procedure was followed for all tests presented in this paper. Before each test the turbines and carriage were held stationary, and a 20 s zeroing measurement was taken to quantify and minimise the influence of sensor drift on the results. For tests with waves, the wave makers were then started, which required some initial ramp-up time. The turbines and carriage were then started at approximately the same instant, with turbine rotational acceleration of 0.523 rad/s^2 and carriage acceleration 0.1 m/s^2, until each met their desired speeds. The turbines were set to both have the same rotational speed, which varied between tests, with the carriage towing speed maintained at 1 m/s for all tests. The time lapse between initiating the wave makers and the carriage motion necessarily varied with wave frequency due to its influence on wave celerity. Although every attempt was made to initiate carriage motion when the approaching wave front was at approximately the same upstream position relative to the parked carriage some variability is inevitable.

Towards the end of the towing tank the turbines and carriage both decelerated, coming to a collective stop around 20 m from the end of the tank. Each towing test lasted approximately 140 s, however due to reflections in the tank, from the waves at the dock end and a turbine-induced bow wave at the wave maker end, the usable data period was shorter than this; see Section 3.3.1. After completing each tow the carriage was reversed at 0.5 m/s to its starting position and a settling time of precisely 15 min maintained until the next tow test.

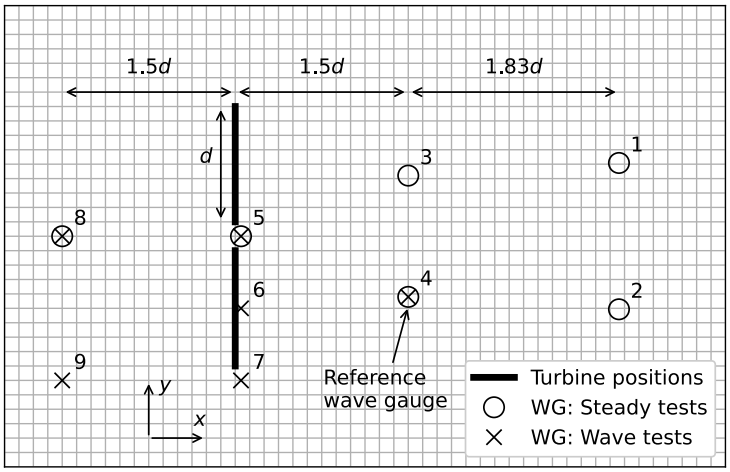

Fig. 1. Wave gauge (WG) positions relative to the turbines; for specific locations see Table 1. The positive x-direction is oriented in the direction of towing, so that waves and relative current travel from right to left.

Table 1
Wave gauge (WG) positions in reference to Fig. 1 with the origin at the rotor plane and at the mid-point between the two rotor centres. The rotor diameter $d = 1.2$ m.

	WG 1	WG 2	WG 3	WG 4	WG 5	WG 6	WG 7	WG 8	WG 9
x/d	3.327	3.327	1.500	1.500	0.050	0.050	0.050	−1.500	−1.500
y/d	0.635	−0.633	0.526	−0.526	0.000	−0.625	−1.250	0.000	−1.250

Wave height was measured with six Pepperl and Fuchs ultrasonic wave probes supplied by the testing facility. All measured channels from the turbine instrumentation and wave gauges were recorded in the same data acquisition system and at the same sampling frequency of 125 Hz to ensure synchronisation. Calibration of the gauges was performed prior to these tests using the same data acquisition hardware and software as used for the turbine-in-wave tests. The calibration showed the wave gauges to be highly linear. Different wave gauge layouts were used for steady tow and combined tow and wave tests as described in Fig. 1 and Table 1.

3. Analysis

3.1. Performance coefficients

Waves cause the turbine thrust $T(t)$ [N] and torque $Q(t)$ [Nm] to fluctuate in time, even when the rotor's rotational speed ω_R [rad/s] is constant. In this work, we define the time-varying thrust and power performance coefficients as:

$$C_T(t) = \frac{T(t)}{\frac{1}{2}\rho U_C^2 A}, \quad C_P(t) = \frac{\omega_R Q(t)}{\frac{1}{2}\rho U_C^3 A} \tag{1}$$

where $A = \pi d^2/4$ is the swept area of each turbine [m^2], ρ is the density of water [kg/m^3], and U_C is the constant current velocity [m/s]. Additionally, we consider two definitions of the tip-speed ratio λ: normalisation of the tip-speed on the constant current velocity U_C; and normalisation of the tip-speed on the instantaneous rotor plane averaged velocity, $U(t) = U_C + U_w(t)$, which includes the combined effects of current and wave-induced horizontal particle velocity $U_w(t)$ (Section 3.2). The two normalisations are defined as:

$$\overline{\lambda} = \frac{\omega_R R}{U_C}, \quad \lambda_D(t) = \frac{\omega_R R}{U(t)} \tag{2}$$

where $R = d/2$ is the rotor radius. The mean tip-speed ratio $\overline{\lambda}$ describes the operating point targeted with turbine control, whereas the dynamic tip-speed ratio $\lambda_D(t)$ reflects the changing flow experienced as a wave passes the turbine.

We note that the wave phase directly influences instantaneous flow speed and rotor loads. In the following sections we describe two approaches to define the wave-phase-varying quantities, either through a single frequency sinusoidal wave fit to the data (Section 3.3.2), or by data binning to create a phase average (see Section 3.3.3).

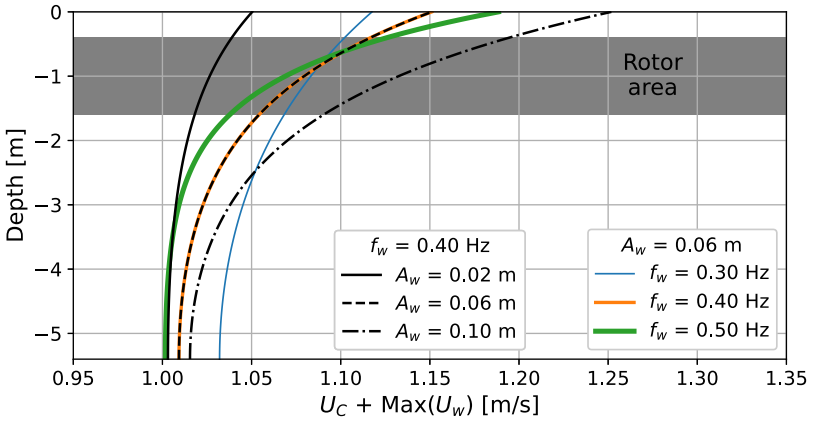

Fig. 2. Depthwise variation in maximum horizontal velocity due to the combined effect of carriage velocity U_C and regular waves U_w for different wave amplitudes and frequencies. The vertical extent of the rotor swept area is annotated for reference.

3.2. Regular waves

The waves generated in the tow tank are assumed to be regular linear waves; measuring the wave-induced velocities was beyond the scope of this work. Consequently, we assume that the depth-varying wave-induced velocity may be directly calculated from the wave amplitude, period, water depth and synchronised with the reference wave measurements defined in Section 4.1. Furthermore, it is assumed that there is no wave–current interaction, as the effective current is realised through the motion of the towing carriage. Utilising the linear wave equations for intermediate water depths, (see for example Journée and Massie, 2001), the surface elevation is described as a function of time t and horizontal position x by:

$$\eta = A_w \sin(\omega_w t - k_w x), \tag{3}$$

with A_w the wave amplitude [m], ω_w the angular wave frequency [rad/s] and k_w the wave number [rad/m]. The horizontal and vertical wave-induced velocity components are given by:

$$U_w = \frac{g A_w k_w}{\omega_w} \frac{\cosh(k_w(z+h))}{\cosh(k_w h)} \sin(\omega_w t - k_w x), \quad V_w = \frac{g A_w k_w}{\omega_w} \frac{\sinh(k_w(z+h))}{\cosh(k_w h)} \cos(\omega_w t - k_w x) \tag{4}$$

where z is the vertical coordinate pointing upwards from the free surface and h is the water depth. Fig. 2 shows the depthwise variation in maximum combined current and wave-induced horizontal velocity for the range of wave amplitudes and frequencies testing in the current experiments. Note that in the turbine frame of reference, the wave encounter frequency is given by $\omega_w^* = \omega_w + k_w U_C$ to account for the Doppler effect, and this modifies the frequency in the trigonometric wave propagation term in Eq. (4).

3.3. Analysis

3.3.1. Time series processing

To study the effect of pure regular waves, a clean time series is required. First, outliers were identified and rejected using a Hampel signal, and then a low-pass filter removed oscillations greater than 10 Hz (4–7 times the rotor rotational frequency depending on the tip-speed ratio of the test). Although each test was conducted for approximately 140 s, only between 20 and 40 s of useful data are identified for each test for further analysis, mainly due to wave reflections and also effects of startup transients from the rotors. Note that the time windows are selected on a case-by-case basis and so there is some potential for unintentional bias, although the suitability of the selection window is discussed in terms of goodness of fit for the harmonic analysis in the following section. The left hand plot in Fig. 3 shows the full time series of the reference wave gauge during a single towing test. The initialisation and ramp up of the wave are clearly visible, followed by some stabilisation before the signal becomes more noisy due to wave reflections; the selected time window of usable data is also shown in the plot. For analysis of the time series two approaches are applied to the windowed time series data; a curve fitting approach analogous to single component harmonic analysis; and phase averaging or data binning. Both approaches are described in the following sections.

3.3.2. Harmonic analysis

Harmonic analysis is applied to signals by fitting a single sinusoidal wave to the time series data. For a given variable $\chi(t)$ this is:

$$\chi(t) = a_\chi \sin(\omega_\chi t + \phi_\chi) + b_\chi \tag{5}$$

with a_χ and b_χ the amplitude of the fluctuating component of the signal and its mean component respectively, and ω_χ and ϕ_χ the angular frequency and phase angle of the signal. For the purposes of this study, this approach is applied to surface elevations and

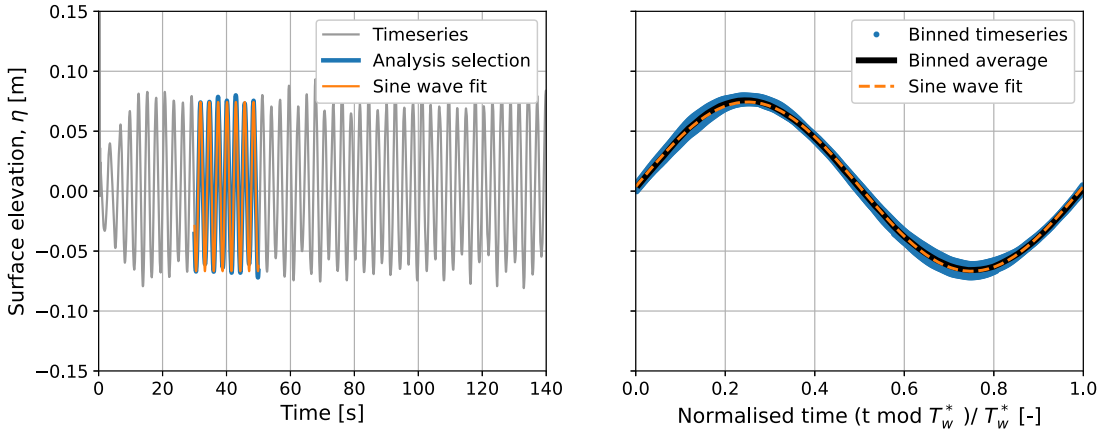

Fig. 3. Example of data selection (left), and phase-averaging over a wave period T_R together with harmonic fitting of a single frequency sine wave to the time series data (right).

the turbine thrust and torque signals only. The single frequency calculated from this method is the relative wave frequency f_w^* (see Section 4.1). Blade signals have additional once per revolution components due to surface passing and cannot be analysed in the same single harmonic manner. As the turbines are controlled to a constant speed harmonic analysis is not applied to the shaft speed.

3.3.3. Data binning

Data binning or phase averaging is accomplished by grouping the time series data into the relevant phase bins and then calculating the mean of the data in each bin. The time signal is grouped into N bins over the relative wave period, as shown by Fig. 3. 72 bins were used over a relative wave period. For the wave frequencies tested, between 1 and 5 sequential time samples were captured by each bin per wave, with several waves used on each test (seven in the example in Fig. 3). Following the harmonic analysis approach, only surface elevation, thrust and torque signals are binned, and the turbine rotational speed is time-averaged.

3.4. Data presentation

The phase differences between the input wave signal and other parameters are of interest in this study. For this reason, in presenting results we adjust the reference wave signal to have zero phase angle ($\phi_\eta = 0$ in Eq. (5)) such that the surface elevation is at the positive crossing ($\eta = 0$) at zero-wave phase angle. All other signals are shifted using the same wave phase angle adjustment, *i.e.*, reported phase angles are relative to the phase of the surface wave.

4. Results

4.1. Realised waves

No calibration was performed on the generated waves prior to testing with the turbines. Rather, the waves were measured during the tests using several wave gauges, shown in Fig. 1. The surface elevation $1.5d$ upstream of one turbine was used as the reference wave probe. From this probe, harmonic analysis is used to determine the measured wave conditions. A comparison of the specified and measured wave conditions is presented in Fig. 4. While a strong relationship is seen between specified and achieved wave frequencies, the measured wave amplitudes show significant deviation from the specified values. Note that the data points used for the amplitude comparison (left plot, Fig. 4) are for the same specified wave frequency, $f_w = 0.5$ Hz, and hence the multiple data points in each vertical column are repeated waves, providing an indication of test repeatability.

The inconsistent agreement between specified and measured wave amplitudes demonstrates the difficulties of performing towing tests in waves. Note that although care was taken to synchronise between the wave makers, carriage start position, carriage start time and turbine control this was manual and approximate, and in particular testing at different wave frequencies presented different arrival times and different required carriage starting times. A testing procedure with greater automation and either a calibration or iteration to improve the generated wave may have provided greater repeatability of test conditions. We note that even in flume environments with waves generated over currents, it can be difficult to match specified and achieved wave conditions with far greater decreases in amplitude (20%–30%) recorded over much shorter distances than in our towing tank experiments (Dufour et al., 2022).

For the remainder of this paper, the measured wave amplitudes and frequencies are used in our analysis. The reference wave signal, measured $1.5d$ upstream of the rotor plane, is propagated in time based on the distance to the rotor plane and the relative velocity of the wave to the approaching turbine, being the sum of the wave celerity and carriage velocity, allowing the reference wave signal to be translated to provide conditions at the rotor that are synchronous with the turbine load measurements. We chose

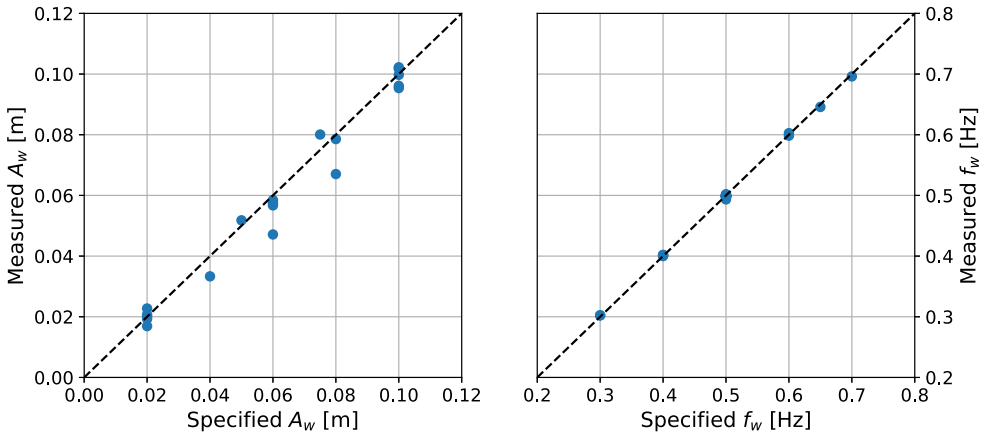

Fig. 4. Amplitude and frequency of measured waves relative to specified conditions. Waves are measured 1.5d upstream of the rotor plane. For amplitude comparison the wave frequency is held constant at $f_w = 0.5$ Hz.

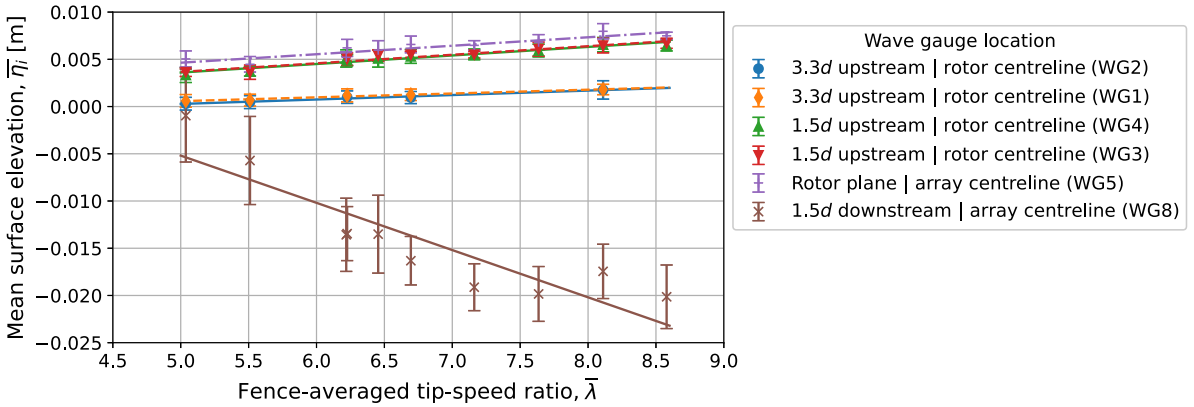

Fig. 5. Measured surface elevations, η_i, under steady flow test conditions. Markers show time-averaged surface elevation and vertical bars represent two standard deviations of the time series.

to use the reference probe 1.5d upstream of the turbine rather than that at the rotor plane as the amplitude of the waves recorded at the rotor plane can be affected by the presence of the rotors. We have tested the accuracy of this approach by comparing the translated measurements of wave gauge 4 with those observed by wave gauge 6. Gauges 4 and 6 are approximately aligned in the transverse direction and the latter is located close to the rotor plane. We find a mean phase difference across all cases of 0.013 rads and a standard deviation of 0.038 rads. This small difference validates our approach and suggests that non-linear interactions between wave propagation and turbine induced velocities ahead of the turbine are negligible for the purposes of this study.

4.2. Influence of the turbines on the free surface

Fig. 5 explores the mean and fluctuating free surface elevation under steady conditions, *i.e.*, without surface waves, at different wave gauge locations as a function of the fence-averaged tip-speed ratio. The turbine fence thrust increases monotonically with tip-speed ratio and provides a resistance to the relative flow that causes a setup in surface elevation ahead of the turbines. The setup decreases with upstream distance ahead of the turbines and is observed to be uniform across the width of the turbine fence. Whilst this effect is relatively small far upstream, 1–2 mm at 3.3d ahead of the turbines, it can reach 5–7 mm at the rotor plane and is therefore non-negligible relative to the range of onset wave conditions to be tested. The setdown in surface elevation downstream of the rotor plane increases with tip-speed ratio and thus resistance to the flow. The vertical bars, representing two standard deviations, show that the time-dependent fluctuations on the free surface elevation are substantially more significant downstream of the two rotors.

Introducing waves, Fig. 6 examines the effect that the test control parameters have on the wave amplitude as waves passes through the array, presented in terms of the ratio of the wave amplitude at each wave gauge position a_i to that of the reference wave, a_0, recorded at wave gauge number 4.

There is no clear dependency of the normalised wave amplitude recorded by the different wave gauges on the reference wave amplitude nor tip-speed ratio. For the tests in which the wave amplitude and tip-speed ratio control parameters are explored, the

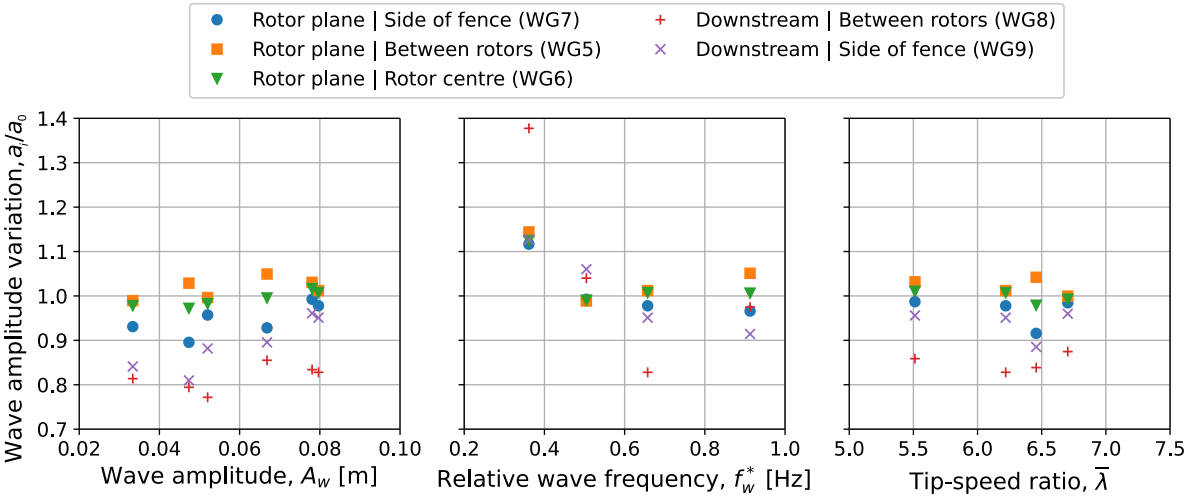

Fig. 6. Normalised wave amplitude variation, a_i/a_0, as a function of test control variables.

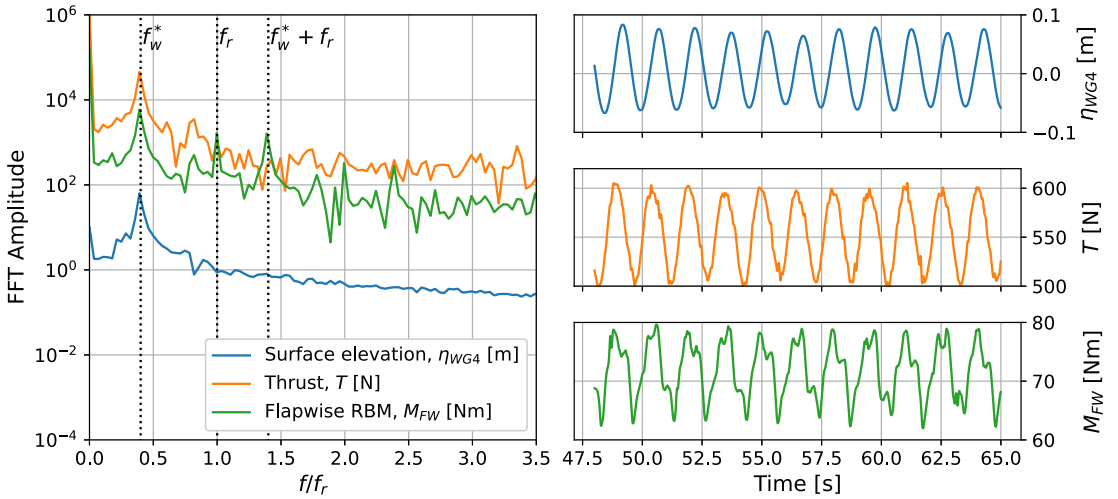

Fig. 7. FFT and time series of wave elevation at wave gauge 4, $\eta_{WG4}(t)$, rotor thrust, $T(t)$, and flapwise blade root bending moment, $M_{FW}(t)$, for a sample test case. Dotted lines denote key frequencies: the relative wave frequency f_w^*, rotor frequency f_r, and their sum frequency. Case shown is $A_w = 0.08\,\text{m}$, $f_w^* = 0.66\,\text{Hz}$, and design tip-speed ratio $\overline{\lambda} = 6.2$.

wave amplitude is observed to reduce between the upstream reference position and the downstream positions, with the gauge between and downstream of the two rotors having a greater overall reduction in amplitude. At the rotor plane there is a reduction in amplitude to the side of the array, but between the rotors the wave amplitude is generally increased by a small amount (up to around 5% of the reference wave amplitude).

A dependency of the wave amplitude on relative wave frequency is observed, showing that the downstream wave amplitude is increased from the reference wave, by 10–15%, for the lower wave frequencies but decreases marginally at higher wave frequencies.

4.3. Performance characteristics

Fig. 7 shows the FFT of several measured signals (wave elevation, rotor thrust, and flapwise root bending moment) for the time series in an example wave test, with the relative wave, rotational, and their sum frequencies highlighted. The relative wave frequency appears as the dominant frequency in all spectra, with the rotational and sum frequencies only featuring significantly in the individual blade bending moments. The single frequency dominance in the turbine thrust confirms the applicability of using single frequency harmonic analysis to represent this signal. For the flapwise blade root bending moment there are multiple clear frequencies present and so a single frequency harmonic representation of the bending moment would not be appropriate.

Fig. 8 shows time- and phase-averaged performance coefficients for a range of TSRs, with the waves at each TSR having approximately the same wave amplitude and frequency. The time-averaged performance coefficients for tests without waves are

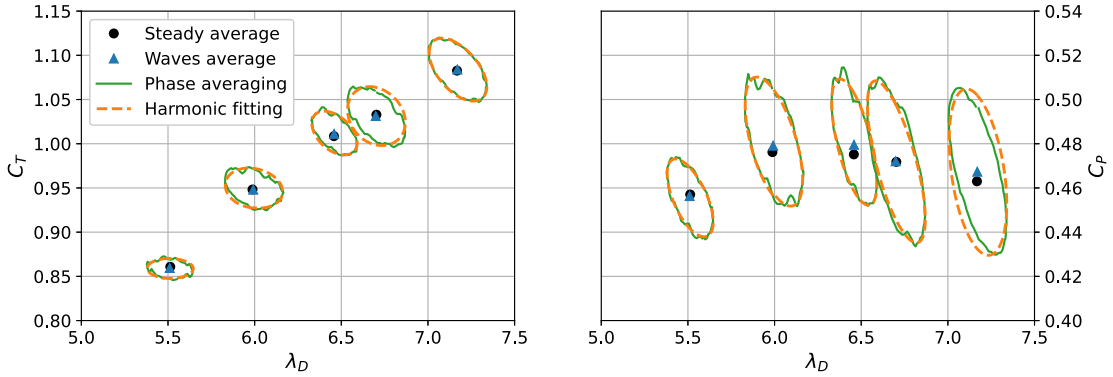

Fig. 8. Performance coefficients, C_T (left) and C_P (right), as functions of instantaneous tip-speed ratio λ_D, for current and combined wave and current conditions ($f_w^* = 0.66$ Hz, $A_w = 0.02$ m). Time- (symbols) and phase- (lines) averaged results shown together with harmonic fitting for combined wave and current cases.

also shown and match closely with the time-averaged performance coefficients from the tests with waves, which is consistent with observations in the literature discussed in Section 1. The phase-averaged wave performance data, here shown with tip-speed ratio normalised based on the instantaneous flow speed, result in hysteresis loops that cycle around the mean at each tip-speed ratio. Performance hysteresis curves created by harmonic fitting, as described in Section 3.3.2, are also shown in Fig. 8. Harmonic fitting generally matches the hysteresis paths generated by phase-averaging, although are smooth as they result from single frequency sine wave approximations, whereas the phase-averaged paths include additional harmonic and non-harmonic components due to turbulence-driven fluctuations and noise.

Fig. 9 shows an annotated example based on harmonic fits to rotor thrust and incident velocity data, via Eq. (5), for the case of $\overline{\lambda} \approx 6.7$ shown in Fig. 8. We use this depiction to help describe the features that make up the hysteresis loops for the performance coefficients. Points where surface elevation η and hence wave-induced horizontal flow speed $U(t)$ are at a minimum/maximum / zero crossing are identified and provide the lateral limits and mean tip-speed ratio crossings for the hysteresis loops.

The thick black line is the baseline data, with the phase difference $\Delta\phi$ defined as the phase angle by which the rotor thrust leads the wave elevation; in this example $\Delta\phi = 78.8°$. Arrows are added to indicate the direction of orbit in $C_T - \lambda_D$ space, with an anti-clockwise orbit (as shown) indicating that the thrust leads the wave elevation, $0° \leq \Delta\phi \leq 180°$, and a clockwise orbit indicating that the thrust lags the elevation, $180° < \Delta\phi < 360°$. A collapse of the hysteresis loop onto a line with a negative gradient would indicate where thrust is in-phase with elevation, shown as $\Delta\phi = 0°$, whilst a loop collapsed onto a line with positive gradient would indicate where thrust and elevation are perfectly out-of-phase, shown as $\Delta\phi = 180°$. Note that these collapsed hysteresis loops need not be straight lines.

Coloured lines highlight the effect of perturbations to the wave and thrust amplitudes. Variations in wave amplitude are associated with changes in the range of the instantaneous tip-speed ratio, whereas variations in the thrust amplitude affect the magnitude of C_T fluctuations.

Returning to Fig. 8, we observe that for a fixed onset wave amplitude and frequency, increasing the turbine's mean tip-speed ratio generally leads to an increase in the fluctuations in both thrust and power coefficient. Further we note that as tip-speed ratio is increased, the phase lead of the thrust fluctuations ahead of the wave elevation reduces as indicated by the rotation of the hysteresis loops in $C_T - \lambda_D$ space: at lowest $\overline{\lambda}$ the ellipse has its major axis nearly horizontal with a phase lead of around 80°, whilst at highest $\overline{\lambda}$ the phase lead is around 20°. The phase lead between power and wave elevation, on the contrary, is much less sensitive to changes in tip-speed ratio, as seen in the lower angular sensitivity of the loops in the $C_P - \lambda_D$ space.

We next examine the influence of wave amplitude on the performance coefficients; see Fig. 10. We consider wave amplitudes $0.02 \leq A_w \leq 0.1$ m at a fixed mean tip-speed ratio close to the design condition, $\overline{\lambda} \approx 6.2$, for two relative wave frequencies, $f_w^* = 0.50$ and 0.66 Hz. The amplitude of coefficient fluctuations increases with wave amplitude due to the larger resulting fluctuations in wave-induced flow speed. The hysteresis loops are not completely elliptical and are sharper at lower instantaneous tip-speed ratios than at higher, indicating larger changes in instantaneous thrust and power at the trough of waves (high λ_D) than at crests (low λ_D). The phase lead remains largely unchanged with varying wave amplitude, but there is clearly some dependency on wave frequency with the narrower loops of the lower frequency case, $f_w^* = 0.50$ Hz, indicating a phase lead closer to 0°.

Focusing on the influence of relative wave frequency for fixed wave amplitude we observe that increasing the relative wave frequency leads to a change in the orientation and aspect-ratio of the hysteresis loops so that torque and thrust lead further ahead of the wave elevation as the relative wave frequency is increased; see Fig. 11. Note in this figure that data are shown for ranges of measured wave amplitudes as the generation of repeatable incident wave conditions was imperfect; see Section 4.1. Decreasing relative wave frequency increases the range of rotor thrust and power coefficient fluctuations, which is likely due to the reduced variation in wave-induced flow speeds with depth across the rotor plane seen at lower wave frequencies, see Fig. 2, which results in greater correlation of fluctuating blade forces across the rotor and thus greater overall rotor force fluctuations.

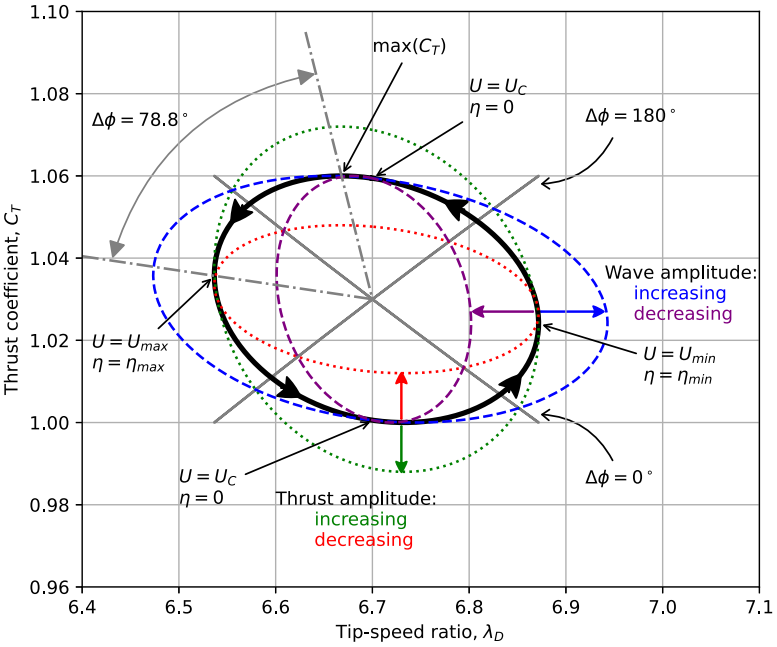

Fig. 9. Annotated exemplar $C_T - \lambda_D$ hysteresis loop depicting fluctuations in wave elevation and thrust. The influence of the phase difference, $\Delta\phi$, by which the thrust leads the wave elevation, is depicted through the angular difference between $\eta_{\max}$ and $\max(C_T)$. The baseline data, indicated by the black line, is the harmonic fit for $\overline{\lambda} \approx 6.7$ in Fig. 8.

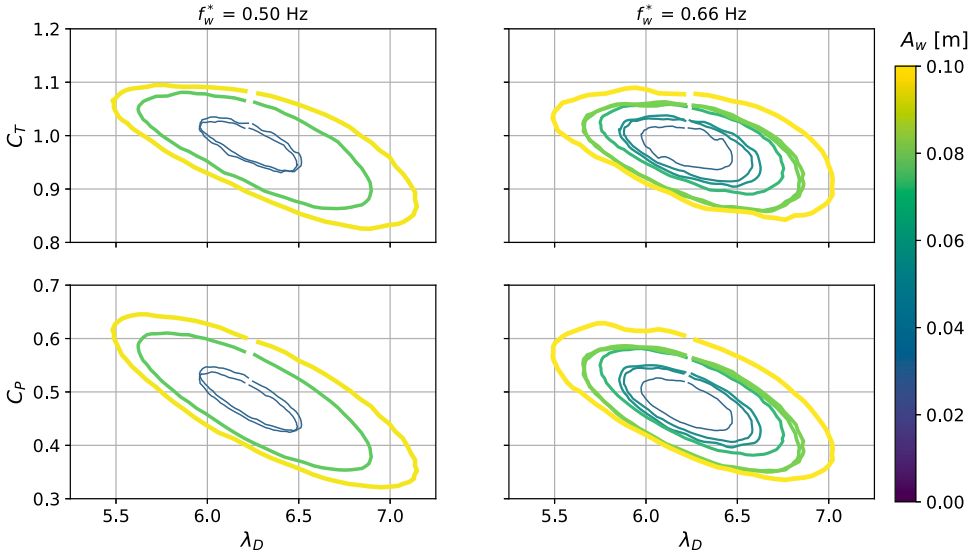

Fig. 10. Influence of wave amplitude, A_w, on phase averaged performance hysteresis loops with the time-averaged tip-speed ratio close to the design condition, $\overline{\lambda} \approx 6.2$, for two wave frequencies, $f_w^* = 0.50$ (left) and 0.66 Hz (right).

4.4. Performance characteristics normalised on instantaneous velocity

An alternative definition for the turbine performance coefficients can be made by normalisation using the instantaneous rotor plane averaged velocity $U(t)$, in place of the carriage speed U_C. Here, we investigate whether a turbine's time-varying performance in waves can be approximated to be quasi-steady using this alternative normalisation. The thrust and power coefficients normalised on instantaneous velocity are defined as:

$$C_{T,D}(t) = \frac{T(t)}{\frac{1}{2}\rho U^2(t) A}, \quad C_{P,D}(t) = \frac{\omega_R Q(t)}{\frac{1}{2}\rho U^3(t) A} \tag{6}$$

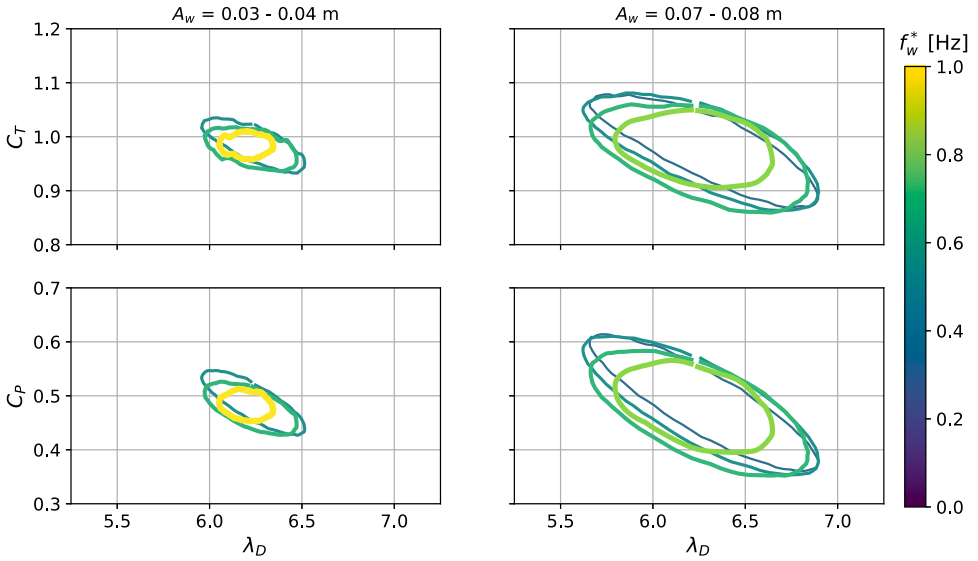

Fig. 11. Influence of relative wave frequency, f_w^*, on phase averaged performance hysteresis loops with the time-averaged tip-speed ratio close to the design condition, $\overline{\lambda} \approx 6.2$, for waves of amplitude 0.03–0.04 m (left) and 0.07–0.08 m (right).

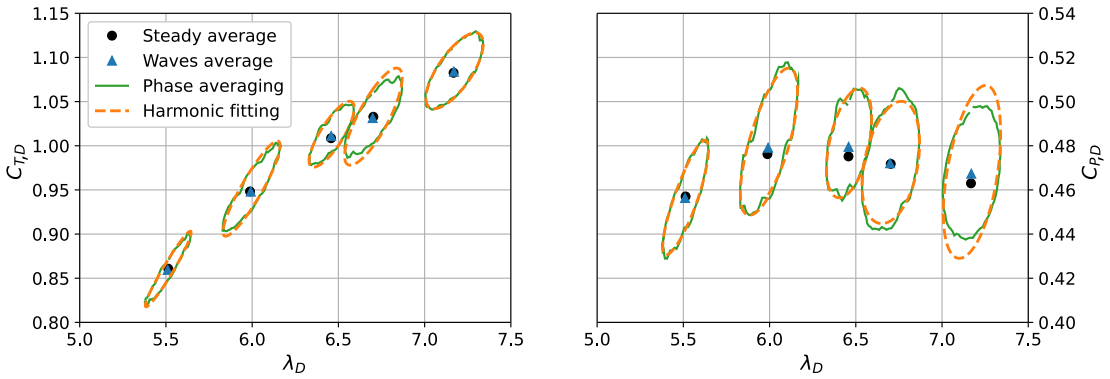

Fig. 12. Instantaneous performance coefficients, $C_{T,D}$ (left) and $C_{P,D}$ (right), as functions of instantaneous tip-speed ratio λ_D, for current and combined wave and current conditions ($f_w^* = 0.66$ Hz, $A_w = 0.02$ m). Time- (symbols) and phase- (lines) averaged results shown together with harmonic fitting for combined wave and current cases.

with $U(t)$ the rotor averaged velocity as discussed in Section 3.

Fig. 12 recasts the cases presented in Fig. 8, but with coefficients normalised on instantaneous velocity. The figure shows time- and phase-averaged $C_{T,D}(t)$ and $C_{P,D}(t)$ for tests with and without waves at different TSRs. As previously observed the time-averaged coefficient data shows little impact of waves as indicated by the negligible departure from the steady flow results, and phase-averaged results appear as hysteresis loops that orbit around the time-averaged coefficients. The shape and orientation of the hysteresis loops are different under this alternative normalisation. The loops do not fall onto a single hypothetical steady state curve, indicating that the wave frequencies tested here are not low enough to justify a quasi-steady approximation to turbine performance.

4.5. Harmonic analysis of wave effects on turbines

In this section the coefficients arising from the harmonic fitting are examined to determine trends and dependencies between the turbine thrust and torque and the control variables of tip-speed ratio, wave amplitude and wave frequency. Correlations of the mean quantities, *i.e.*, b_χ in harmonic analysis, see Eq. (5), are well understood in the literature. Here we focus on the amplitude of the load fluctuation with respect to its mean, a_χ/b_χ, and phase difference between the load and reference wave, ϕ_χ.

Fig. 13 explores the phase and normalised amplitude for the turbine's thrust and torque as a function of the test control variables. The variation of the normalised amplitudes of both torque and thrust correlate approximately linearly with the variation in the control variables. As observed from the hysteresis loops discussed in the previous section, the fluctuating force coefficients show a strong positive dependency on wave amplitude, and a weaker negative dependency on wave frequency, for the range of amplitudes

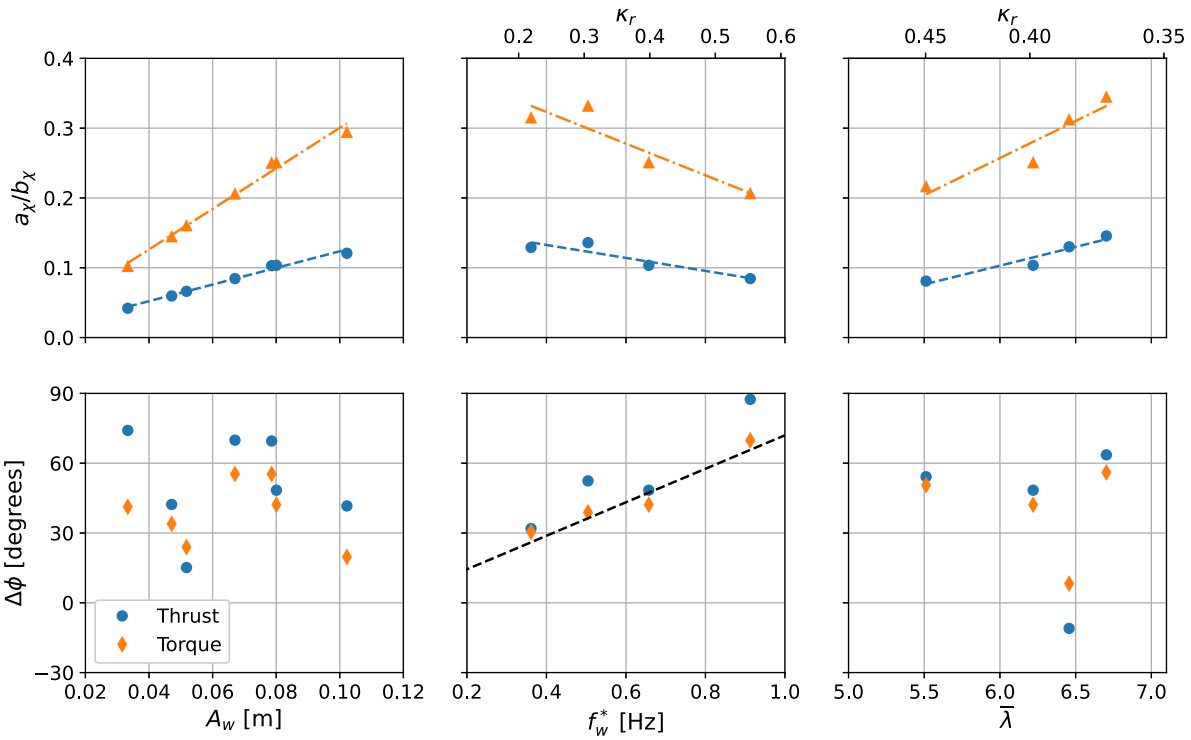

Fig. 13. Influence of control parameters, wave amplitude, relative wave frequency and tip-speed ratio on normalised fluctuation amplitude and phase of performance coefficients. To investigate dependency on each control variable the remaining controls are held approximately fixed at values of $A_w = 0.08\,\text{m}$, $f_w^* = 0.66\,\text{Hz}$ and $\overline{\lambda} \approx 6.2$ as required.

and frequencies tested. The dependency on mean tip-speed ratio is positive and similar in range to that experienced over the range of wave frequencies tested. Relative fluctuation amplitudes are greater for torque than thrust as are the rates of change of the fluctuation amplitudes with the control variables.

For the relative wave frequency and tip-speed ratio controls, the reduced frequency $\kappa_r = f_w^*/f_r$, is shown as an additional axis. We observe that for the same change in κ_r, the magnitude of the thrust and torque variations differ depending on the control variable used to alter κ_r. Hence, κ_r is not able to uniquely parameterise the amplitudes of the fluctuating loads. This demonstrates potential issues in applying this non-dimensional parameter to the global analysis. By varying wave frequency, and hence relative wave frequency, the wave-induced velocity profile changes (see Eq. (4)) and so achieving similar κ_r values with different wave frequencies, can result in different velocity profile depth decays that then lead to different force fluctuations across the rotor.

Thrust and torque lead the wave elevation with thrust generally exhibiting a greater phase lead. There is little observable consistent change in phase with wave amplitude, hence the constant slope and aspect-ratio of the ellipses in Fig. 10. There is, however, a strong positive correlation observed between phases and wave frequencies, and hence the rotation of the ellipses in Fig. 11 as f_w^* is increased.

4.6. Blade loading

In this section we discuss how the wave amplitude and frequency affect the blade root bending moments in both flapwise and edgewise directions. The global performance coefficients, discussed in previous sections, are a summation of loads from three blades at different positions and hence obscure variations as the blades rotate. The blades, however, experience incident flow variation due to the time-variation of the wave field and the vertical variation of the wave kinematics profile. To investigate the effect on blade loads as they rotate through incident waves, we apply a binning approach whereby root bending moments are sorted and binned according to both blade azimuth angle and relative wave phase. To maximise usable data over the limited number of rotations per test, load data are compiled from all three blades and a coarse binning is applied with 16 bins in wave phase and 8 bins in blade azimuth. This process was followed for each incident wave amplitude and frequency tested. It is worth highlighting that following the processing many datasets remained incomplete due to missing data in some bins; the results presented here are for subsets of wave tests which have complete data for both turbines and load directions. We measure blade azimuth angle, ψ, from top dead centre in the direction of blade rotation (anti-clockwise as viewed from upstream of the turbines), and wave phase, ϕ_w, from upwards crossing of the mean surface level.

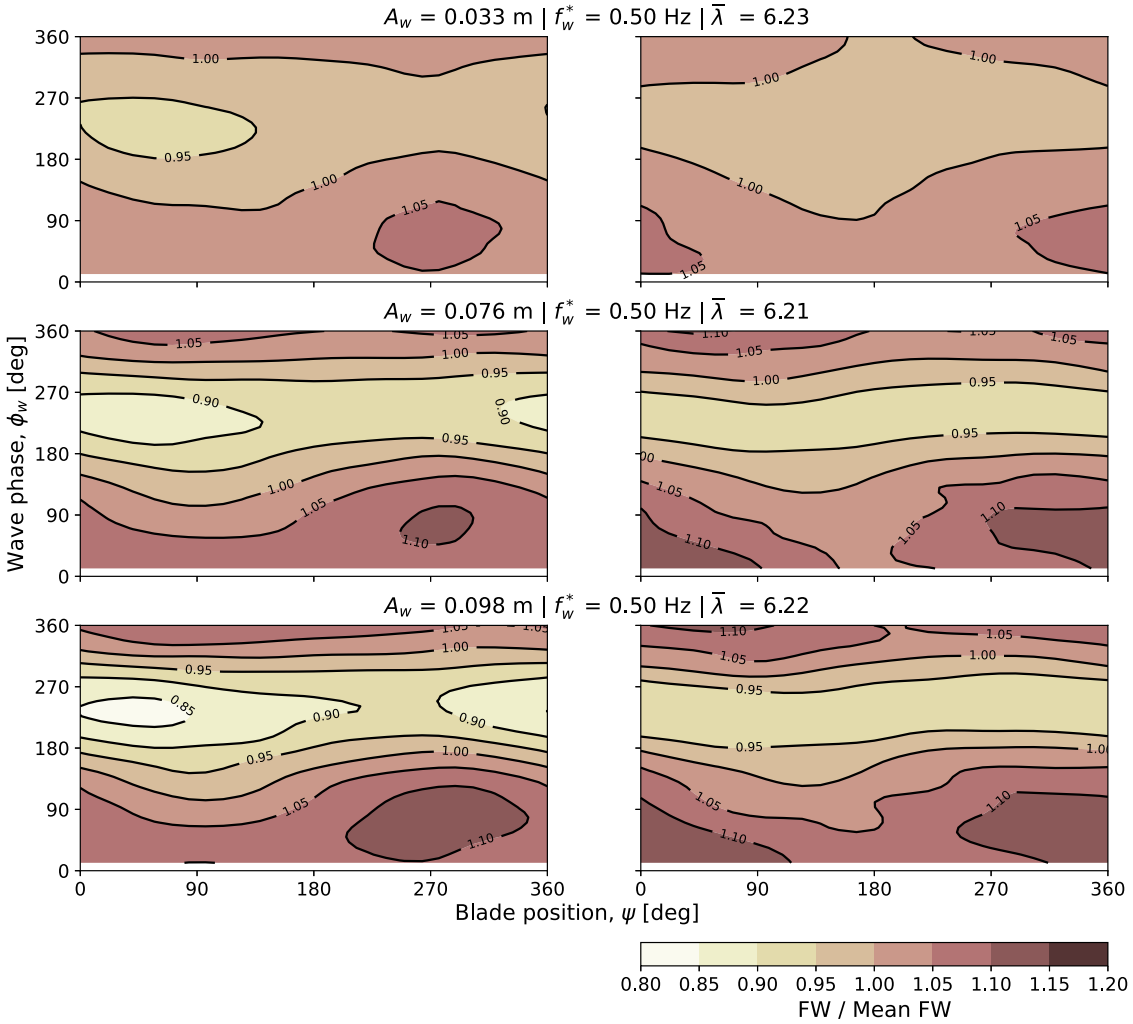

Fig. 14. Effect of wave amplitude on flapwise (FW) root bending moment as function of blade azimuth position, ψ, measured from top dead centre, and wave phase, ϕ_w, measured from the upwards crossing of the mean surface level. Left and right plots correspond to left- and right-side rotors. Bending moments are shown normalised by the mean bending moment recorded for that test condition.

The influence of wave amplitude is explored in Figs. 14 and 15 for flapwise and edgewise loading respectively for both rotors and for a fixed wave frequency. It is evident that the blades exhibit significant fluctuations in both directions: ±15% in flapwise and ±35% in edgewise around mean values and that these fluctuations grow with wave amplitude and therefore wave kinematics, as might be expected.

The roughly horizontal bands running across the contour plots indicate that the blade loads in both directions are maximised when the wave is ascending and the surface is approaching maximum elevation, 30–90° wave phase, and are minimised when the wave is descending towards the wave trough, 210–270° wave phase. At these wave phases for maximum and minimum load we observe azimuthal variations in loads with peak flapwise loads occurring when the blade is on the upstroke at around 270° and minimum when the blade is on the downstroke at around 90°. The azimuthal locations of maximum and minimum flapwise bending moments are more distinct for the left-hand rotor that the right-hand rotor, which is believed due to turbine-turbine hydrodynamic interaction effects. The blade phases for maximum and minimum loads in the edgewise direction are similar for both rotors, and are located at approximately 90° and 270° of blade phase, opposite to the positions of maximum and minimum flapwise bending moments.

At first these results would seem contrary to expectations, as one might expect the largest loads when blades are vertical around top dead centre and experience their maximum wave-induced flow speeds. However, the wave-induced velocities decay rapidly with depth and therefore so do the wave-induced perturbations to the blade local angle-of-attack. Furthermore, the resistance presented by the rotor will locally modify the wave-induced velocities in a non-linear depth-dependent manner that will likely provide an additional mechanism by which angle-of-attack will vary along the blade length when vertical. We theorise that the depth decay and resistance modification to wave orbitals results in a blade that, whilst in steady flow experiences a near uniform angle-of-attack

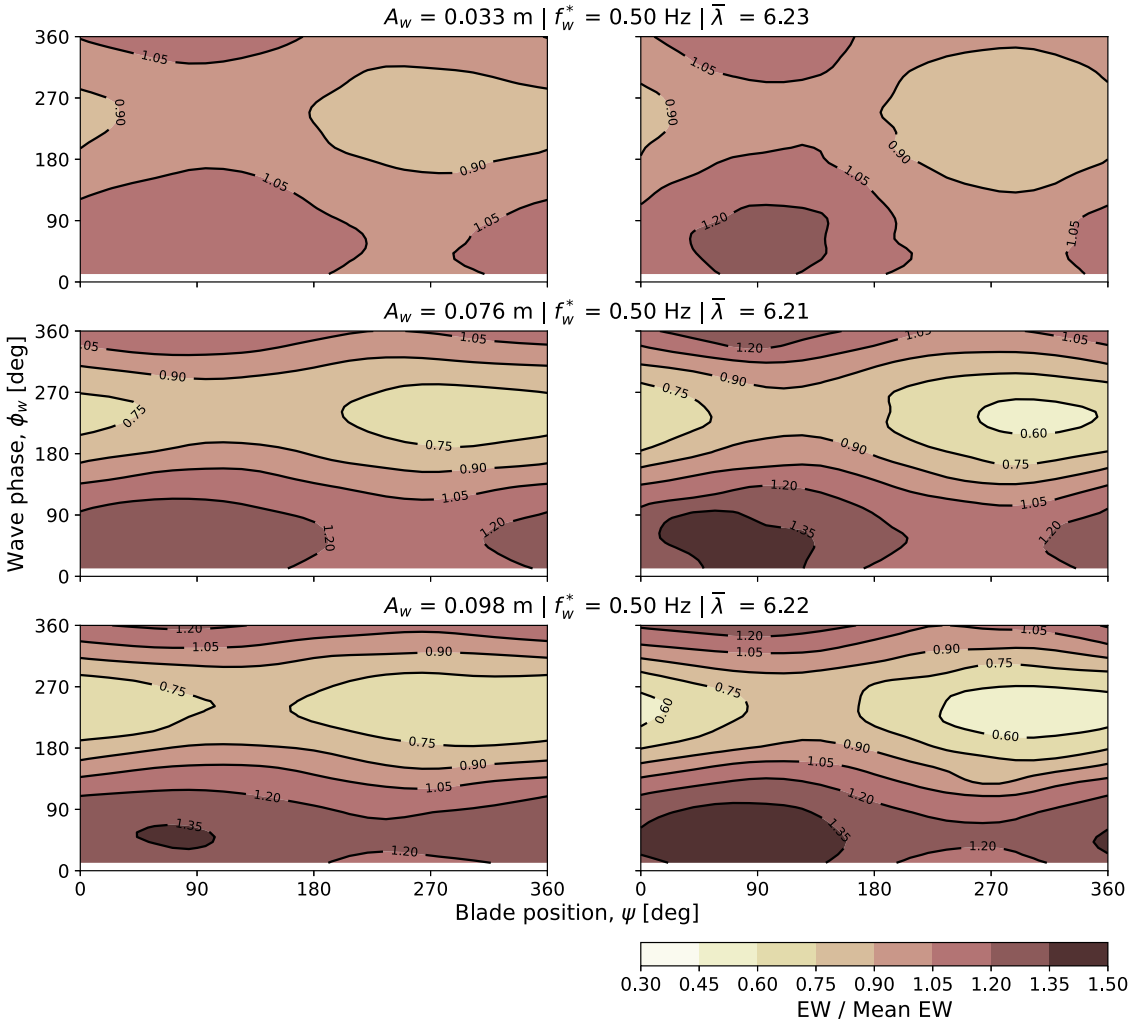

Fig. 15. Effect of wave amplitude on edgewise (EW) root bending moment. See caption of Fig. 14 for further details.

along its length (as discussed by Cao, 2020), may now experience a highly varying angle-of-attack along its length when vertical, depending on the intensity and rate of decay of wave-induced kinematics with depth. This variation leads to blade load fluctuations that are de-correlated along the blade span when around the vertical position, with the outer sections of the blade experiencing larger fluctuations and being more likely to stall. Therefore, blade load maxima (and minima) do not necessarily occur at vertical blade azimuth positions.

As the blade rotates towards the horizontal it will experience an approximately constant wave-induced velocity along its span. This leads to a broadly similar increase (at wave crest $\phi_w \approx 90°$) or decrease (at wave trough $\phi_w \approx 270°$) in wave-induced velocity, which is well correlated along the blade span when blades are in the downstroke around $\psi \approx 90°$ or upstroke around $\psi \approx 270°$. This in turn leads to well correlated wave-induced force fluctuations along the blade span when the blade is around horizontal azimuth positions, and hence the occurrence of maxima and minima at these blade positions. Note that even if the wave-induced velocity perturbation is exactly constant along the blade span it will still result in a spanwise varying wave-induced perturbation in angle-of-attack due to the non-linearity of the blade local velocity triangle and contributions from blade rotation and induced velocities.

The two rotors experience differences in wave-induced fluctuations with the right-hand rotor experiencing greater fluctuations in edgewise loads and the left-hand rotor greater fluctuations in flapwise loads. These differences are believed to stem from the hydrodynamic interactions between the two rotors and differences in the approaching direction of blades to wave-induced velocities. Recall that both rotors spin in the same direction, and so interference effects between the two rotors will not be symmetric around the vertical as might be expected for side-by-side counter-rotating rotors. The azimuthal locations of load maxima (and similarly opposing minima) have been investigated previously for steady flow conditions. For a single turbine of the same blade design as in this study, the maximum flapwise and edgewise blade loads in a sheared flow were observed as the blade approaches the top

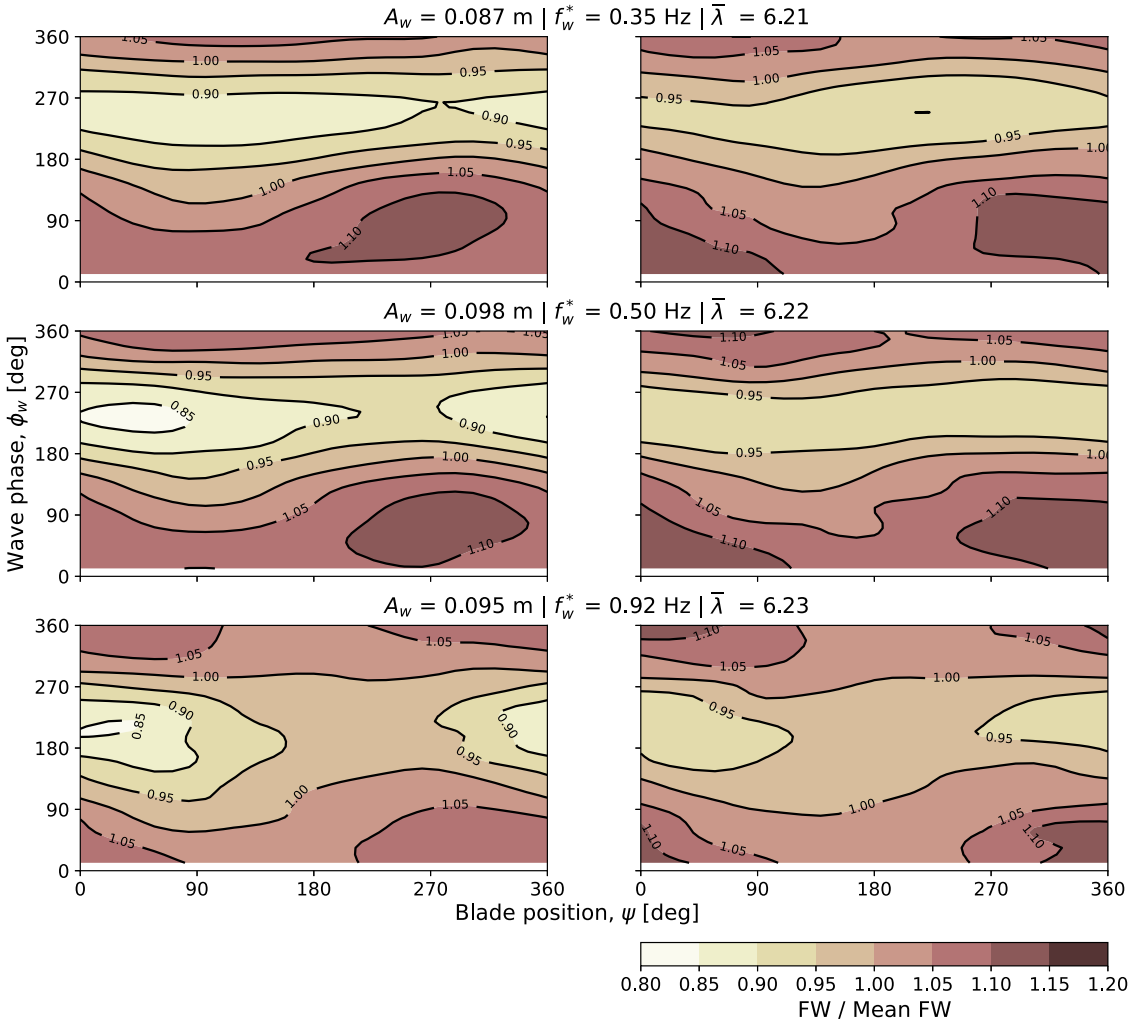

Fig. 16. Effect of wave frequency on flapwise (FW) root bending moment. See caption of Fig. 14 for further details.

position (310–315°) and the minimum after it passes the bottom-most position (McNaughton et al., 2022). In towed tests the same co-rotating side-by-side turbines positioned at the same inter-turbine spacing as the current tests, experienced load amplifications when blades were close to horizontal and passing by the neighbouring turbine. For blade passing effects in steady flow edgewise loads peak around the horizontal whilst flapwise loads peak around 10–30° before the blades reach the horizontal when approaching from either above or below (McNaughton et al., 2023).

The rotor blades interact in a non-symmetric manner between upstrokes and downstrokes due to the blade interaction with the incoming wave. Whilst the horizontal component of wave-induced velocity affects the angle-of-attack across the entire blade azimuth, the vertical component of wave kinematics, which is in quadrature with the horizontal component, only affects the incidence when blades are away from the vertical, with maximum effect when blades are in the horizontal position. At any given wave phase the vertical component of wave kinematics will act in opposite directions (with and against rotor rotation) on the opposite sides of the rotor ($\psi \approx 90°$ and $\psi \approx 270°$). This implies that vertical wave kinematics can induce non-symmetric loads with respect to blade phase.

We conclude that the complex nature of the loading variation with respect to blade azimuth and wave phase is due to many factors, with maxima and minima occurring at wave crests and troughs but when blades are horizontal so that wave effects correlate along blade spans. Differences in which loads, flapwise or edgewise, experience maxima or minima on downstrokes and upstrokes are likely due to vertical wave kinematics, with secondary effects from rotor-rotor interactions, as well as due to non-linear effects not captured by a simple velocity triangle view of the blade incident velocity, such as stall and three-dimensional flow effects.

We next examine the influence of wave frequency on the azimuthal and wave phase variation of the fluctuating flapwise and edgewise bending moments; see Figs. 16 and 17. Note that as before, due to the imprecision of controlling the measured wave amplitude just ahead of the turbines, the variation with wave frequency is made for conditions of approximately constant wave

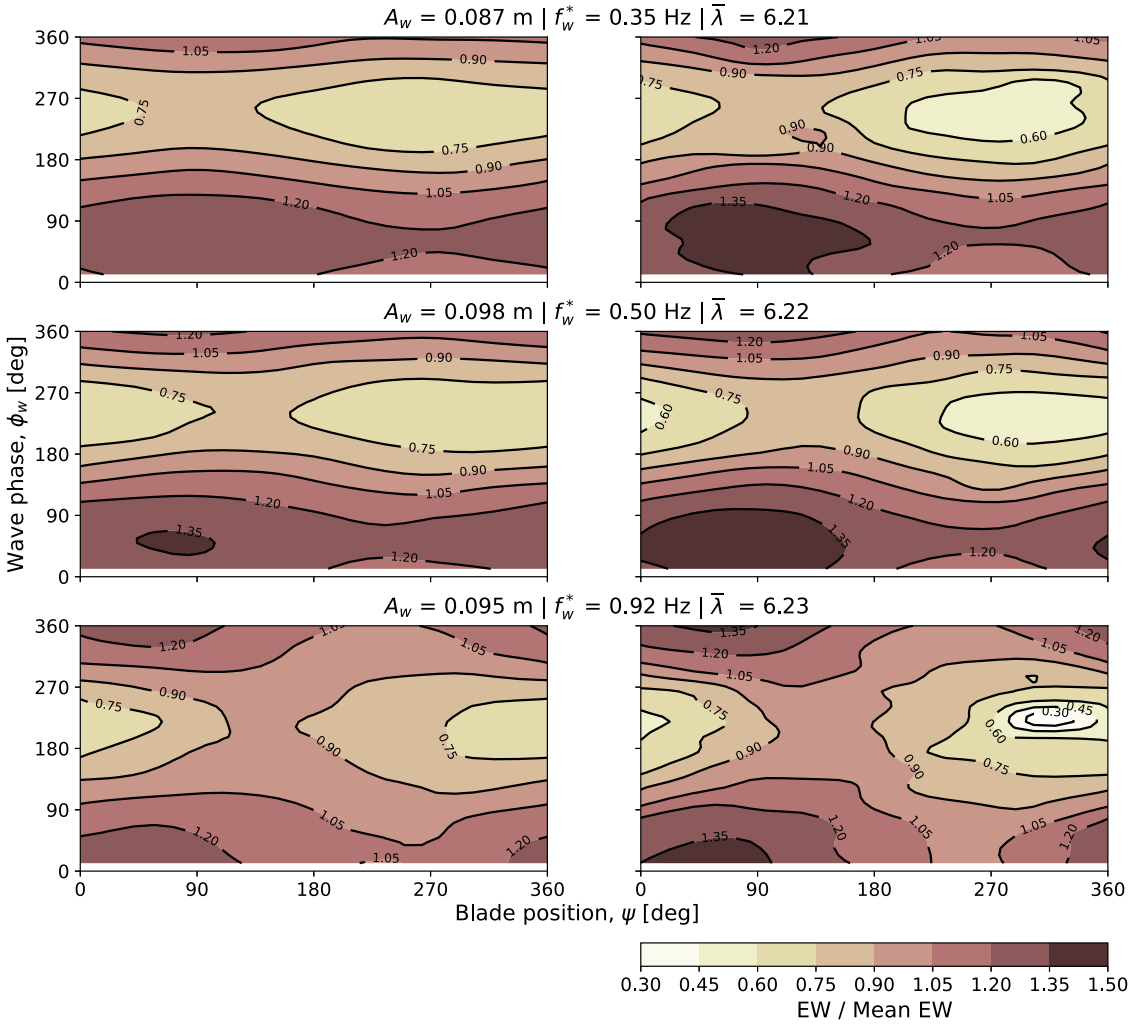

Fig. 17. Effect of wave frequency on edgewise (EW) root bending moment. See caption of Fig. 14 for further details.

amplitude. We observe that, for the cases analysed, changing the wave frequency has some, but less pronounced, effects on the magnitude of fluctuating bending moments than changes in the wave amplitude, which is consistent with the influence of wave amplitude and frequency on whole rotor thrust and torque fluctuations, see Fig. 13. Also consistent with the sensitivity of whole rotor loads is the modest reduction in the amplitude of the flapwise bending moment as wave frequency is increased. Changes in the amplitude of edgewise fluctuations with wave frequency are less clear and may be complicated by the small changes in wave amplitude between different wave frequencies considered, with torque/edgewise loads generally being more sensitive to changes in conditions than thrust/flapwise loads, again see Fig. 13 for whole rotor sensitivities.

Changes to the wave frequency lead to changes in the location of maximum and minimum bending moments which occur, with increasing wave frequency, at decreasing wave phase as the wave elevation is rising but ahead of the crest, and as the wave elevation is falling but ahead of the trough. The azimuthal locations of maximum and minimum bending moments are also affected by wave frequency with increasing frequency leading to both maximum and minimum flapwise and edgewise bending moments occurring closer to top dead centre blade locations as wave crests and troughs are approached respectively. Recall that as wave frequency is increased the wave-induced velocity decays more rapidly with depth and so the wave-induced velocity at hub height is reduced, see Fig. 2. It appears that the increase in wave frequency is such that the wave-induced velocities when the blade is in the horizontal position are no longer significant enough to deliver maximum and minimum fluctuating loads at these locations. Instead the blades now see instantaneous shear flow conditions under rising and falling waves where blade loads peak just before or after top dead centre which is similar to the behaviour that is observed in steady flow vertically sheared conditions (McNaughton et al., 2022).

5. Conclusion

This paper reports on experiments on two side-by-side 1.2 m diameter tidal stream turbines in currents and regular waves in a large scale towing tank laboratory experiment. The paper analyses mean and fluctuating components of whole rotor torque and thrust as well as contributions to blade bending moments. For the case without waves it is found that the presence of the turbines causes a setup in the approaching flow surface together with a setdown downstream of the turbines, and that the magnitude of these disturbances increase with tip-speed ratio and therefore turbine resistance. The setup is non-negligible, around 5 mm at 1.5 diameters upstream of the rotors, and must therefore be accounted for in the characterisation of the measured approaching waves upstream of the turbines. Tests were conducted over a range of tip-speed ratios from 5.5 to 7.1 around the turbine's design point of 6.2, in steady current conditions with and without regular head waves of amplitude up to 100 mm and encounter frequencies over the range 0.35 Hz to 0.92 Hz.

The time-mean power and thrust coefficients of the turbines when tested in waves aligned well with the steady flow power and thrust coefficients recorded without waves, in agreement with observations in the literature from previous experiments. Dynamic fluctuations around the time-mean coefficients were found in waves with the load path forming a hysteresis loop around the time-mean result in the force coefficient-dynamic tip-speed ratio plane with the latter defined based on the rotor face-averaged instantaneous velocity which necessarily changes through the wave cycle. The hysteresis loops are approximately elliptical in shape with their orientation and aspect-ratio indicating the phase lead between the forces and the wave elevation. Simple single harmonic fits to forces and elevation were found to be useful for whole turbine results, enabling phase to be established, but could not be applied to individual blade loads which experience fluctuations at both rotation and wave frequencies as well as sum frequencies.

Increasing wave amplitude was observed to expand the elliptical hysteresis load paths in an approximately linear manner with unsteady torque fluctuations increasing faster than unsteady thrust fluctuations. Increasing wave frequency was found to have a more complex effect on turbine loads leading to a reduction in unsteady load amplitudes, again with greater reductions in unsteady components of torque than thrust, and an increase in the phase lead of the fluctuating components over the wave elevation. Increasing turbine tip-speed ratio for the same onset wave condition leads to increased turbine fluctuating loads and a reduction in the phase by which thrust leads elevation, but less change in the phase by which torque leads. The fluctuating whole rotor loads recorded were large and up to 35% of the time-mean loads. By re-normalising thrust, power and tip-speed ratio using the dynamic rotor face-averaged velocity it was not possible to collapse rotor performance curves on to steady state curves and hence we conclude that for the range of wave frequencies tested here, a quasi-steady flow approximation to estimate dynamic rotor loads cannot be made.

Blade loads are influenced by the azimuth position and wave phase. Maximum and minimum flapwise and edgewise loads are found to occur as the wave is rising towards its crest, wave phase angles of 30° to 90°, and falling towards the wave trough 210° to 270°. However, contrary to expectations these maxima and minima do not occur when blades are top dead and bottom dead centre, at azimuthal positions of 0° and 180°, but when blades are in the horizontal positions. We postulate that this is due to the homogeneity of wave orbitals that occurs along the span of blades when they are horizontal leading to well-correlated fluctuations in angle-of-attack and loads along blade spans. Whilst when blades are vertical the decay of wave particle orbits with depth leads to non-homogeneous wave-induced velocities over blade spans leading to large uncorrelated fluctuations in angle-of-attack and loading along the blade span, and although these fluctuations may be large, particularly at the tips of blades when top dead centre, the spanwise decorrelation of these fluctuating loads means that vertical azimuth positions are not the locations of maximum blade root bending moments. We find that flapwise and edgewise maximum (and minimum) loads occur on opposite sides of the rotor with flapwise loads maximised on the upstroke at azimuth angles of around 270°, whilst edgewise loads are maximised on the downstroke, azimuth of around 90°, and we attribute this to the vertical component of wave-induced velocities which, for a given wave phase, is additive to the blade section relative velocity on one side of the rotation, and reduces the relative velocity on the other side. As wave frequency is increased the wave orbitals decay more rapidly with depth and the maxima seen when blades are horizontal under correlated wave orbitals at lower wave frequencies no longer occur. At higher wave frequencies the maximum and minimum blade root bending moments, in both flapwise and edgewise directions, occur closer to top dead centre as the blades now experience maximum shear flow type conditions under wave peaks and troughs. The load patterns of the two side-by-side rotors show some differences which we attribute to hydrodynamic interaction effects.

CRediT authorship contribution statement

J. McNaughton: Writing – review & editing, Writing – original draft, Methodology, Investigation, Formal analysis, Conceptualization. **F. Zilic de Arcos:** Writing – review & editing, Formal analysis. **C.R. Vogel:** Writing – review & editing, Formal analysis. **R.H.J. Willden:** Writing – review & editing, Supervision, Methodology, Investigation, Formal analysis, Conceptualization.

Declaration of competing interest

The authors declare that they have no known competing financial interests or personal relationships that could have appeared to influence the work reported in this paper.

Acknowledgements

The authors would like to acknowledge the UK EPSRC for their support in funding this work through RHJW's fellowship, grant no. EP/R007322/1. Additionally, CRV would like to acknowledge the support of the UKRI through his Future Leaders Fellowship MR/V02504X/1, and FZdA would like to acknowledge funding from the European Union's Horizon 2020 research and innovation programme under the Marie Skłodowska-Curie grant agreement no. 101034329, recipient of the WINNINGNormandy Programme supported by the Normandy Region. JM would like to thank Sam Tucker Harvey, Daniel Rowe and Daniel Dehtyriov for contributing to the experimental testing, and Mark McAllister for helpful discussions during the analysis.

Data availability

Data will be made available on request.

References

Adcock, T.A.A., Draper, S., Willden, R.H.J., Vogel, C.R., 2021. The fluid mechanics of tidal stream energy conversion. Annu. Rev. Fluid Mech. 53, 287–310.

Allmark, M., Martinez, R., Ordonez-Sanchez, S., Lloyd, C., O'Doherty, T., Germain, G., Gaurier, B., Johnstone, C., 2021. A phenomenological study of lab-scale tidal turbine loading under combined irregular wave and shear flow conditions. J. Mar. Sci. Eng. 9 (6), 593. http://dx.doi.org/10.3390/jmse9060593.

Barltrop, N., Varyani, K.S., Grant, A., Clelland, D., Pham, X.P., 2007. Investigation into wave-current interactions in marine current turbines. Proc. Inst. Mech. Eng. Part A: J. Power Energy 221 (2), 233–242.

Cao, B., 2020. Hydrodynamic design of multi-rotor tidal array (Ph.D. thesis). University of Oxford.

Draycott, S., Payne, G., Steynor, J., Nambiar, A., Sellar, B., Venugopal, V., 2019. An experimental investigation into non-linear wave loading on horizontal axis tidal turbines. J. Fluids Struct. 84, 199–217.

Draycott, S., Steynor, J., Nambiar, A., Sellar, B., Venugopal, V., 2020. Rotational sampling of waves by tidal turbine blades. Renew. Energy 162, 2197–2209.

Dufour, M.-A., Gaurier, B., Pinon, G., Germain, G., Facq, J.-V., Togneri, M., Represas, F., Nicolas, E., Marcille, J., 2022. Comparison of the experimental response of two horizontal axis tidal turbines to wave and current. In: 25ème Congrès Français de Mécanique-CFM 2022.

Faudot, C., Dahlhaug, O.G., 2012. Prediction of wave loads on tidal turbine blades. Energy Procedia 20, 116–133.

Galloway, P.W., Myers, L.E., Bahaj, A.S., 2014. Quantifying wave and yaw effects on a scale tidal stream turbine. Renew. Energy 63, 297–307.

Gaurier, B., Davies, P., Deuff, A., Germain, G., 2013. Flume tank characterization of marine current turbine blade behaviour under current and wave loading. Renew. Energy 59, 1–12.

Guo, X., Yang, J., Gao, Z., Moan, T., Lu, H., 2018. The surface wave effects on the performance and the loading of a tidal turbine. Ocean Eng. 156, 120–134. http://dx.doi.org/10.1016/j.oceaneng.2018.02.033.

Journée, J.M.J., Massie, W.W., 2001. Offshore Hydromechanics, first ed. Delft University of Technology.

Li, Z., Ghia, K., Li, Y., Fan, Z., Shen, L., 2021. Unsteady Reynolds-Averaged Navier-Stokes investigation of free surface wave impact on tidal turbine wake. Proc. R. Soc. A 477 (2246), 20200703.

Lust, E.E., Luznik, L., Flack, K.A., Walker, J.M., Van Benthem, M.C., 2013. The influence of surface gravity waves on marine current turbine performance. Int. J. Mar. Energy 3–4, 27–40. http://dx.doi.org/10.1016/j.ijome.2013.11.003.

Luznik, L., Flack, K.A., Lust, E.E., Taylor, K., 2013. The effect of surface waves on the performance characteristics of a model tidal turbine. Renew. Energy 58, 108–114.

McNaughton, J., Cao, B., Nambiar, A., Davey, T., Vogel, C.R., Willden, R.H.J., 2022. Constructive interference effects for tidal turbine arrays. J. Fluid Mech. 943, A38. http://dx.doi.org/10.1017/jfm.2022.454.

McNaughton, J., Ettema, S., Zilic de Arcos, F., Vogel, C.R., Willden, R.H.J., 2023. An experimental investigation of the influence of inter-turbine spacing on the loads and performance of a co-planar tidal turbine fence. J. Fluids Struct. 118, 103844. http://dx.doi.org/10.1016/j.jfluidstructs.2023.103844.

Nishino, T., Willden, R.H.J., 2012. The efficiency of an array of tidal turbines partially blocking a wide channel. J. Fluid Mech. 708, 596–606.

Ouro, P., Mullings, H., Christou, A., Draycott, S., Stallard, T., 2024. Wake characteristics behind a tidal turbine with surface waves in turbulent flow analyzed with large-eddy simulation. Phys. Rev. Fluids 9, 034608.

QinetiQ, 2018. Towing Tank. URL https://www.qinetiq.com/-/media/ec7b7352798047c1bf0f7cd73949048c.ashx.

Scarlett, G.T., Sellar, B., van den Bremer, T., Viola, I.M., 2019. Unsteady hydrodynamics of a full-scale tidal turbine operating in large wave conditions. Renew. Energy 143, 199–213.

Sørensen, J.N., Shen, W.Z., 2002. Numerical modeling of wind turbine wakes. J. Fluids Eng. 124 (2), 393–399.

Stallard, T., Mullings, H., Draycott, S., Ouro, P., 2023. Large-eddy simulations of interaction between surface waves and a tidal turbine wake in a turbulent channel. In: Proceedings of the European Wave and Tidal Energy Conference, Vol. 15.

Zilic de Arcos, F., McNaughton, J., Vogel, C.R., Pinon, G., 2023a. A study on tidal rotors under the combined effects of currents and waves using actuator-line CFD simulations. In: Proceedings of the European Wave and Tidal Energy Conference, Vol. 15.

Zilic de Arcos, F., Vogel, C.R., Willden, R.H.J., 2023b. A numerical study on the hydrodynamics of a floating tidal rotor under the combined effects of currents and waves. Ocean Eng. 286, 115612. http://dx.doi.org/10.1016/j.oceaneng.2023.115612.

Zormpa, M., Zilic de Arcos, F., Chen, X., Vogel, C.R., Willden, R.H.J., 2025. The effect of flow sampling on the robustness of the actuator line method. Wind Energy 28, e2965.